INTERNATIONAL JOURNAL OF HYDROGEN ENERGY 42 (2017) 14786–14793

Available online at www.sciencedirect.com

ScienceDirect

journal homepage: www.elsevier.com/locate/he

Role of lattice strain and texture in hydrogen embrittlement of 18Ni (300) maraging steel

M. Béreš [a], L. Wu [b], L.P.M. Santos [a,c], M. Masoumi [a], F.A.M. da Rocha Filho [a], C.C. da Silva [a], H.F.G. de Abreu [a], M.J. Gomes da Silva [a,*]

[a] Federal University of Ceará, Department of Metallurgical and Materials Engineering, Campus do Pici, Av. Humberto Monte, CEP 60445-554, Fortaleza, CE, Brazil

[b] Brazilian Nanotechnology National Laboratory – LNNano, CNPEM, R. Giuseppe Máximo Scolfaro 10000, CEP 13083-970, Campinas, SP, Brazil

[c] Federal University of Ceará, Department of Analytical Chemistry and Physical Chemistry, Campus do Pici, Av. Humberto Monte, CEP 60451-970, Fortaleza, CE, Brazil

ARTICLE INFO

Article history:
Received 3 November 2016
Received in revised form
27 March 2017
Accepted 29 March 2017
Available online 12 May 2017

Keywords:
Maraging steel
Hydrogen-induced crack
EBSD
Lattice strain
Synchrotron X-ray diffraction

ABSTRACT

Hydrogen embrittlement causes engineering components to fail unexpectedly. Maraging 300 steel was hydrogen charged and subjected to slow strain rate tensile test until fracture. Electron backscatter diffraction analysis of fractured specimen revealed that cracks initially propagated intergranulary along prior-austenite grain boundaries. When cracks faced martensitic $\{111\}\alpha$ planes parallel to normal direction (ND) they were deflected and continued to propagate transgranulary through $\{001\}\alpha$//ND planes. Finally, cracks were arrested by $\{111\}\alpha$//ND planes. Crystallographic planes on which cracks propagate/are arrested, correlate well with planes that exhibit highest/lowest magnitude of lattice strain determined during tensile loading using *in situ* synchrotron X-ray diffraction.

© 2017 Hydrogen Energy Publications LLC. Published by Elsevier Ltd. All rights reserved.

Introduction

High-strength maraging steels are extensively used in the nuclear power, chemical processing and aerospace industries, in applications where they are susceptible to hydrogen embrittlement (HE) [1–11]. The HE is typically characterised by a significant loss of tensile ductility and causes engineering components to fracture unexpectedly. It can be affected by microstructure, hydrogen content, strain rate, temperature, level of applied stress in addition to magnitude of residual stress [8,12–15]. The most common hypotheses that are used to explain the HE mechanism include (i) hydrogen-enhanced vacancy clusters formation [16], (ii) hydrogen-induced decohesion [17] and (iii) hydrogen-enhanced localised plasticity (HELP) [18]. In case of martensitic maraging steels, the later mechanism is the predominant failure mode [19]. This mechanism is based on the accumulation of hydrogen at

* *Corresponding author.*
E-mail address: mgsilva@ufc.br (M.J. Gomes da Silva).
http://dx.doi.org/10.1016/j.ijhydene.2017.03.209
0360-3199/© 2017 Hydrogen Energy Publications LLC. Published by Elsevier Ltd. All rights reserved.

dislocations, precipitates and grain boundaries [20]. Dissolved hydrogen enhances dislocation mobility and reduces number of available slip systems because the cross slip is hindered [12,21]. Since the deformation becomes more localised, in that region the propensity for cracking is enhanced [21]. When exposed to hydrogen, high-strength steels may fail either by intergranular separation along the prior-austenite grain boundaries [22] or by transgranular fracture along planes which traverse the prior-austenite grains [23]. Intergranular, quasi-cleavage, or microvoid coalescence fracture modes can operate depending upon the microstructure, the crack-tip stress intensity, the concentration of hydrogen and dislocation interactions with grain boundaries [8,12]. Intergranular decohesion can be caused by the grain boundary segregation of impurity elements and hydrogen [24]. The transgranular fracture in body-centred cubic (BCC) crystals involves the separation of atomic bonds along low-index {001} crystallographic planes which are considered energetically favourable due to their low surface energy [25]. According Qiao and Argon [26], as cleavage crack propagation occurs in two adjoining grains a crack propagates in the first grain and is arrested by the grain boundary. With the increased applied stress cleavage microcracks are induced in the second grain along the {001} facets. Then, microcracks propagate along the cleavage facets of the second grain until bridging the cleavage crack in the first grain and break the grain boundary. Finally, the crack continues to propagate in the second grain with its perturbed crack front.

Although crystallographic texture is likely to reduce hydrogen-induced cracking because it can determine availability of low resistance paths for crack propagation [27–31] a limited work has been conducted to date. An understanding of crystallographic texture and load interaction effects at a crack-tip can play a key role in improvement of HE resistance of critical engineering components.

Recently, Venegas et al. [28,29,32] demonstrated that high resistance to HE can be achieved through tailoring of texture. In these studies, a low carbon steels with crystallographic texture dominated by $\{001\}\alpha//ND$ fibre was prone to HE due to the availability of low resistance cleavage paths. In contrast, texture composed of $\{112\}\alpha//ND$, $\{111\}\alpha//ND$ and $\{011\}\alpha//ND$ fibres was less susceptible to HE.

When a polycrystalline material is subjected to deformation, slip occurs initially in grains orientated favourably with the load axis. The neighbour grains, aligned in unfavourable orientation for slip, will experience local load increase generating intergranular microstrain [33]. Neutron or synchrotron X-ray diffraction can be used to study lattice strains in a polycrystalline material from the shift of the diffraction peaks [34,35].

This work examines the role of lattice strain accumulation in individual crystallographic planes on hydrogen-induced crack propagation in maraging steel. We measured the lattice strain in maraging steel using synchrotron X-ray diffraction during *in situ* tensile loading and found correlation between lattice strain and crack propagation. The results obtained can be used to better understand the damage mechanism caused by hydrogen and for improvement of the material's resistance to hydrogen-induced crack propagation.

Experimental

The studied material was commercial maraging steel grade 300 containing 18.7% Ni, 9.6% Co, 4.8% Mo, 0.9% Ti, balance Fe (wt.-%). Cylindrical tensile test samples with a gauge length of 28 mm and diameter of 4.1 mm were machined from a forged bar 300 mm in diameter. The specimens were subjected to solution annealing at 820 °C for 1 h followed by air cooling to ambient temperature and then ageing treatment at 480 °C for 3 h and air cooling. The heat treated samples were then grounded using SiC paper with mesh size up to 1200, followed by polishing with 6, 3 and 1 μm diamond paste. Finally, they were etched with Marble's reagent consisting of 10 g $CuSO_4$ + 50 ml HCl + 50 ml distillated water [36] and examined using Olympus® BX-51M optical microscope. X-ray diffraction measurements were carried out on the heat treated samples using a Philips® X'Pert Pro diffractometer. Step scan mode with step size 0.013°, time per step 100 s and angular interval 10–120° was applied. Cu K_α radiation (wavelength of 0.154 nm) was used in addition to operating voltage and current of 40 kV and 45 mA, respectively. In order to minimize the texture effect a spinner holder was used.

The heat treated samples were cathodically charged for 24 h prior to loading and during the on-going slow strain rate test in aqueous 0.6 M NaCl electrolyte. For the hydrogen charging, a potential of −1.2 V_{SCE} according the ASTM G129-00 and ASTM F1624-09 standards [37,38] was applied. The slow strain rate tests were conducted using a strain rate of 1.0×10^{-6} s^{-1} in a Cortest® tensile test machine. Further experimental details of this test can be found in work carried out by Santos et al. [39]. Relative strength and ductility losses were chosen to identify HE susceptibility.

Synchrotron X-ray diffraction was used to measure the lattice strain accumulated in different crystallographic planes during tensile loading. This test was performed on specimens without hydrogen charging, which were subjected to identical heat treatment as shown in the previous section. For *in situ* determination of the lattice strain, samples with cross-section of 4×4 mm^2 were deformed to failure at room temperature in tension in the Gleeble Thermomechanical Simulator integrated within the XTMS beamline at the Brazilian Synchrotron Light Laboratory, in Campinas. The Gleeble system operated in stroke control mode, with macroscopic force applied to the sample recorded using a 44 kN load cell. The tensile specimens were positioned perpendicular to the diffraction beam, continuously loaded to a selected stroke using a strain rate of 1×10^{-3} s^{-1} and held for ~300 s. A monochromatic X-ray beam with dimensions at the slit system of 2.0×0.5 mm^2 and wavelength of 1.0332 Å (12 keV) was used to illuminate the sample during loading. Then a scan in angular range of 21–83° (covering an interplanar *d*-spacing range of 0.78–2.83 Å) was acquired before a subsequent stroke step was applied. The diffraction patterns were acquired using two silicon microstrips MYTHEN one-dimensional detectors. The instrument parameters were obtained using Al_2O_3 powder standard. A laser dilatometer was used to record changes in sample cross section at gauge centre during straining.

The measured data consisted of a series of diffraction patterns as function of applied load and strain. The positions

of diffraction peaks were found by performing a Gaussian peak fit using the Matlab program with a peak-fitting script written by beamline staff. Lattice d-spacings for each peak were obtained from the diffraction spectra during tensile loading. For each analysed peak, the lattice strain ε^{hkl} can be determined from the measured lattice spacing d^{hkl} (strained lattice) and a reference lattice spacing d_0^{hkl} which is the measured lattice spacing at zero load (unstrained lattice). The lattice strain was then calculated according ref. [35]:

$$\varepsilon^{hkl} = \frac{d^{hkl} - d_0^{hkl}}{d_0^{hkl}} \quad (1)$$

Microstructural examinations were performed by secondary electron imaging (SEI) and electron backscattering diffraction (EBSD). Samples for EBSD analysis were prepared on the fractured surface perpendicular to the load axis. Standard metallographic preparation method consisting of mechanical polishing and final polishing with colloidal silica suspension was used. Crystal orientation maps were obtained using EBSD system mounted on a FEI® Quanta FEG 450 scanning electron microscope (SEM) equipped with HKL Oxford NordlysNano® camera utilising the Aztec acquisition software. The acquired EBSD data were analysed using Oxford Instruments HKL Channel 5 software. The ARPGE (Automatic Reconstruction of Parent Grains from EBSD data) software package [40] was used to reconstruct prior-austenite grains from the martensite orientations measured by EBSD. The reconstructed prior-austenite grains and pole figures were then plotted in the HKL Channel 5 software. Orientation distribution functions (ODFs) were calculated from EBSD maps in regions ahead and around crack tip using the MTEX software package [41]. Fracture surfaces of samples were examined using a FEI® Quanta FEG 450 SEM operated at 20 kV.

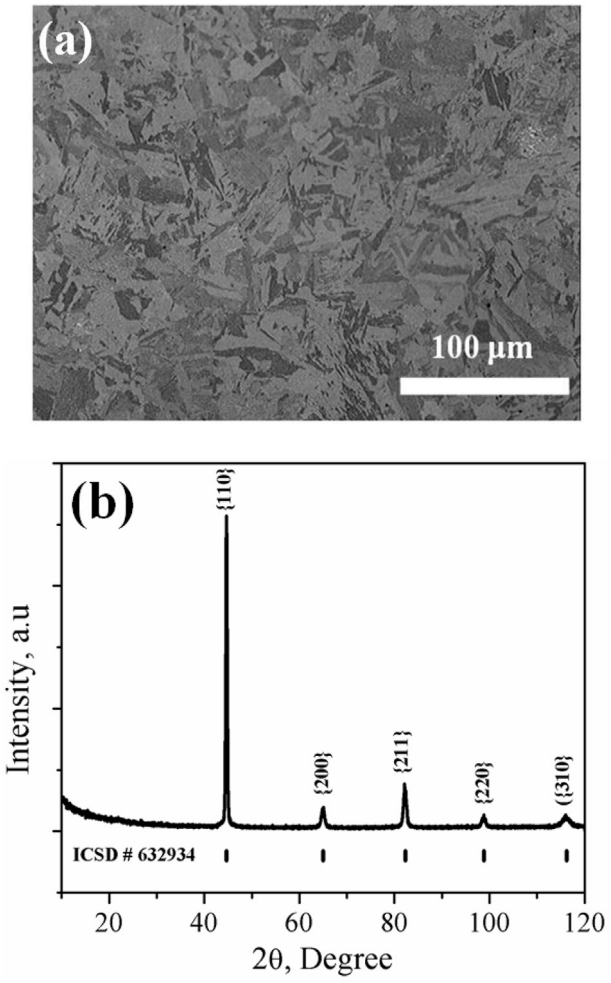

Fig. 1 – (a) Optical micrograph of maraging steel solution annealed at 820 °C for 1 h and aged at 480 °C for 3 h. (b) X-ray diffraction patterns of the same sample showing BCC phase only.

Results and discussion

The microstructure of the maraging steel grade 300 which was subjected to solution annealing at 820 °C for 1 h followed by ageing treatment at 480 °C for 3 h is presented in Fig. 1a. The massive martensite blocks are visible and consist of parallel laths. Fig. 1b shows X-ray diffraction results of the same sample. Diffraction patterns match well with body-centred cubic structure, ICSD file card 632934, space group Im3m (#229). It is to be noted that no presence of austenite was identified from the diffraction peaks.

The slow strain rate tensile tests under hydrogen charging induced HE in maraging steel successfully. Fig. 2 shows engineering stress–strain curves for both hydrogen charged samples and specimens tested in air. An ~8% strain was measured in the sample tested in air (after onset of necking), whereas the charged specimen failed at ~0.3% strain only, without occurrence of necking. Mechanical properties obtained from the slow strain rate tensile test are presented in Table 1. The measured low level of deformation in hydrogen charged specimen can be attributed to hydrogen accumulated at grain boundaries which will decrease their cohesive strength due to the dislocation-grain boundary interactions that can lead to enhanced slip transfer at lower stresses [12]. In Fig. 3 a low magnification SEM fractograph of hydrogen charged specimen with primary hydrogen-induced crack is

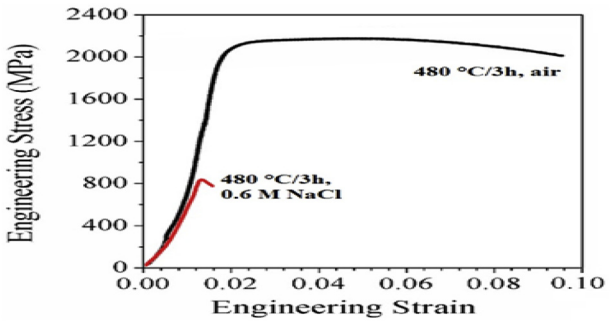

Fig. 2 – Engineering stress–strain curves for samples hydrogen charged (red curve) and tested in air (black curve) obtained from slow strain rate tensile test. (For interpretation of the references to colour in this figure legend, the reader is referred to the web version of this article.)

Table 1 – Mechanical properties of maraging steel aged at 480 °C for 3 h obtained from slow strain rate tensile test. Specimens were tested in air and hydrogen charged in 3.5% NaCl aqueous solution under −1.2 V_{SEC} at room temperature. In this Table the symbols mean; δ: elongation; ψ: reduction in area of cross section; HE = $[(X_{air} - X_{3.5NaCl})/X_{air}] \times 100$, where X is property under investigation.

Medium	UTS (MPa)	δ (%)	ψ (%)	HE – UTS (%)	HE – δ (%)	HE – ψ (%)	Time to fracture (h)
Air	2180	8.0	41.8	–	–	–	22.2
3.5% NaCl	840	0.3	2.1	61.5	96.2	95.0	0.83

shown. Fig. 4a shows a higher magnification SEM fractograph of the specimen aged at 480 °C for 3 h and tested in air where a ductile transgranular fracture mode with non-uniform dimples containing inclusions is present. The non-uniform dimples distribution is typical for a microvoid coalescence fracture mechanism where voids nucleate at inclusions or second-phase precipitates. Viswanathan et al. [42] identified manganese, titanium and sulphur rich particles on the fracture surface of 18% Ni maraging steel. A dispersoid free surface was observed in the smaller dimples. SEM fractograph of the hydrogen charged specimen revealed intergranular fracture in addition to transgranular ductile fracture mode, as shown in Fig. 4b. Also quasi-cleavage regions were observed and these are displayed in the inset micrograph of Fig. 4b. The change in fracture mode may be related with the direction of crack propagation and slip transmission across a grain boundary [12].

Fig. 5a shows an inverse pole figure EBSD map from a metallographic section, perpendicular to the tensile direction, through a fracture surface of hydrogen charged specimen and HE-induced crack. Experimentally determined crystallographic orientations were used to reconstruct prior-austenite grains employing the ARPGE software [40] considering the Nishiyama–Wassermann (NW) orientation relationship. Fig. 5b shows results of this reconstruction. One can see that in this region only two prior-austenite grains 1 (green) and 2 (red) were found and the crack propagated along them. The obtained Euler angles for prior-austenite grains 1 and 2 were 198.6°, 38.8°, 78.2° and 339.4°, 10.5°, 54.2°, respectively. It is known that martensitic laths accumulate hydrogen and act as fracture nucleation sites where they intersect with prior-austenite grain boundaries [43]. Ohtani and McMahon [44] describe that the austenitic grain boundaries that were formed at high temperature form a coarse polygonal network in which the dihedral angles are approximately 120°. If a crack propagates along this network, it will be deflected through an average angle of 60° on a triple junction. The energy required to induce an intergranular fracture increases with frequency and severity of such deflections. If the austenite transforms into martensite, the dihedral angles of the martensitic packet and block boundaries are much larger than 60°. In addition, the martensitic packet and block units are smaller in size in comparison to the prior-austenite grains. Therefore, higher energy is required for crack propagation along martensite.

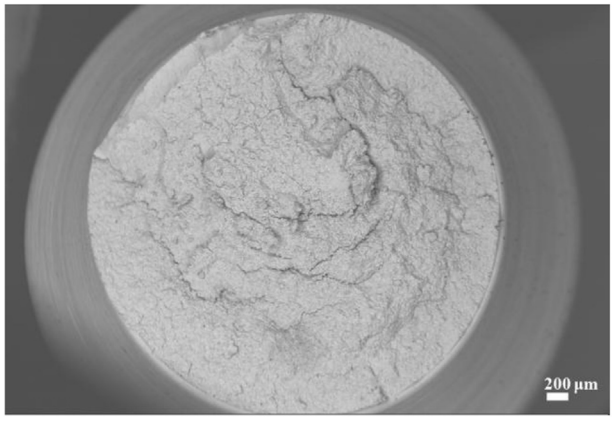

Fig. 3 – A low magnification SEM fractograph of a hydrogen charged specimen showing hydrogen-induced primary crack.

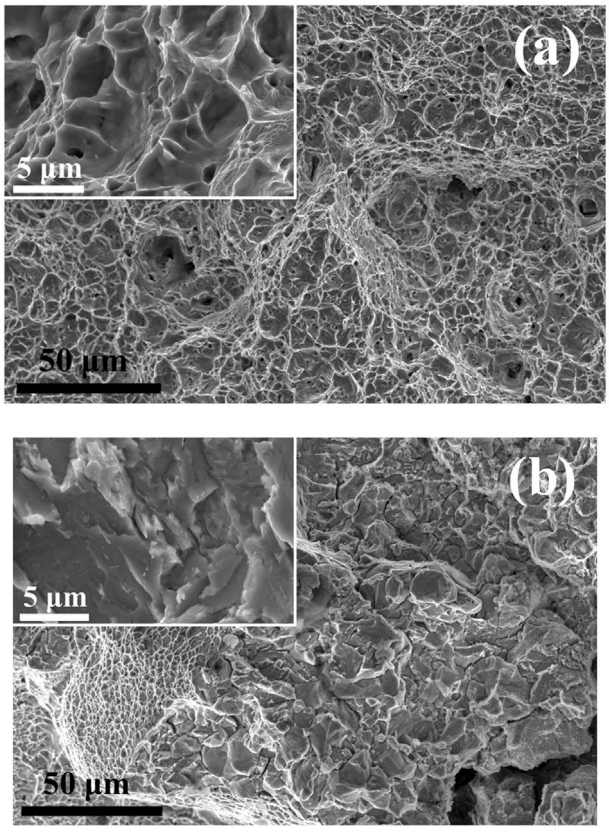

Fig. 4 – (a) SEM fractograph of specimen tested in air shows a transgranular fracture mode with non-uniform dimples. (b) SEM fractograph of hydrogen charged specimen shows mixture of intergranular and ductile transgranular fracture mode. A quasi-cleavage fracture was also observed. Higher magnification of the fracture surface is shown in the inset micrographs.

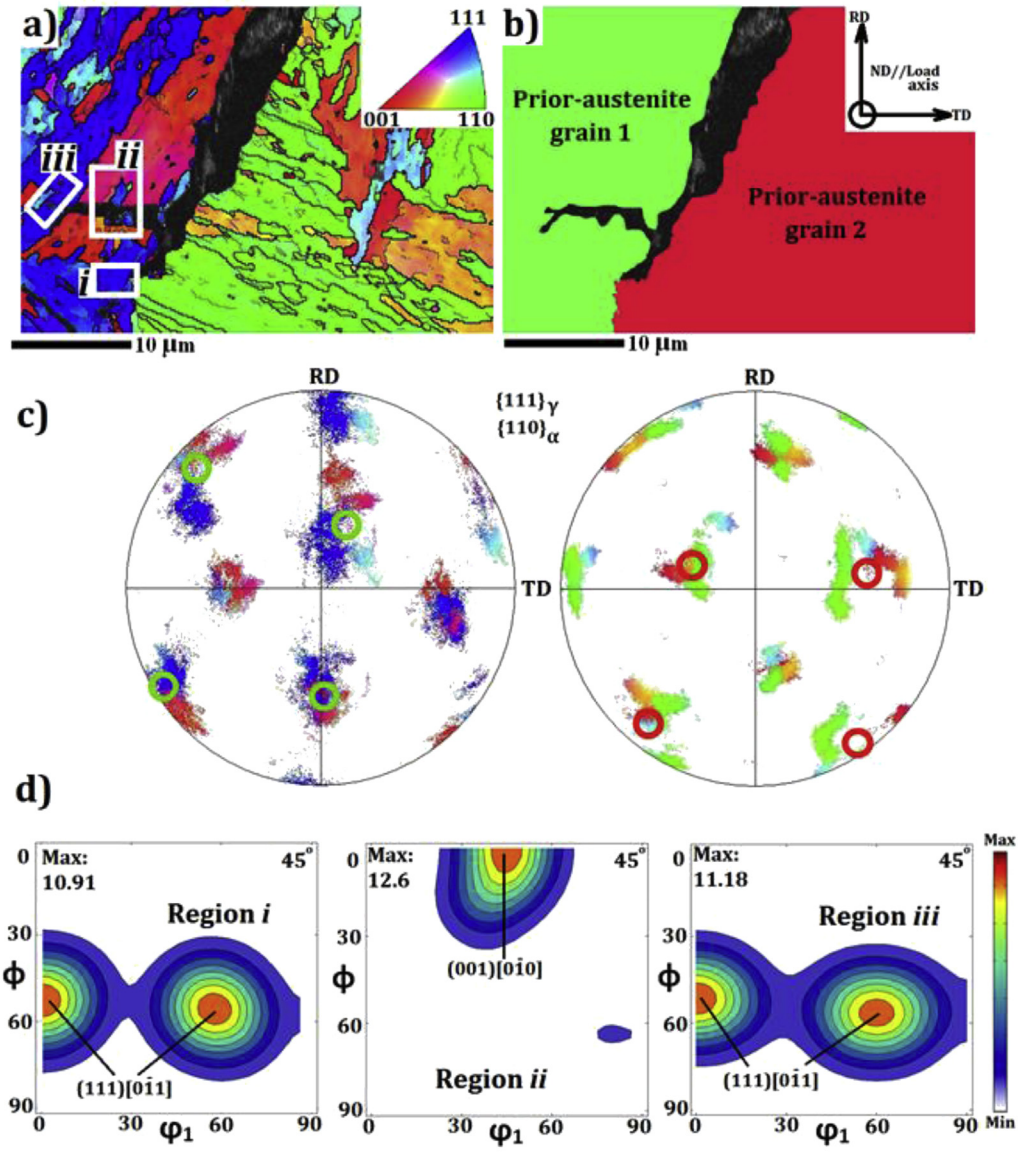

Fig. 5 – (a) EBSD inverse pole figure map showing martensite with hydrogen-induced crack. (b) EBSD inverse pole figure map showing reconstructed prior-austenite grains 1 and 2 obtained from experimental orientation in (a) considering NW orientation relationship. (c) $\{111\}\gamma$ pole figures of grains shown in (b) depicted with green and red circle for prior-austenite grains 1 and 2, respectively. Also superimposed are $\{110\}\alpha$ pole figures from experimentally determined orientations in corresponding areas in (a). Please note that the colours correspond to the orientation shown in (a). (d) Calculated orientation distribution function from regions depicted with white boxes in (a). (For interpretation of the references to colour in this figure legend, the reader is referred to the web version of this article.)

An additional reason to favour intergranular fracture is segregation of alloying elements on grain boundaries. Fracture surfaces of prior-austenite grain boundaries in 300 grade maraging steel tested under hydrogen were examined by Auger electron microscopy [45]. This study revealed that the alloying elements including nickel, molybdenum and titanium segregate to prior-austenite grain boundaries, which were defined as primary fracture path. Austenite grain size can influence the extent of intergranular embrittlement because smaller grains lead to a greater grain boundary area. As a consequence, the grain boundaries are less enriched with impurities and the material is then less susceptible to HE. Thermomechanical treatment can be used to tailor prior-austenite grain size. Fuchigami et al. [46] demonstrated that the refinement of the prior-austenite grain size increased the hydrogen absorption capacity as a consequence of the increased boundary area which led to reduction of susceptibility to HE.

Figueroa and Robinson [47] examined hydrogen charged 300M martensitic steel and attributed the HE to retained austenite at prior-austenite grains. However, X-ray diffraction patterns did not revealed presence of austenite, Fig. 2.

Fig. 5c presents {111}γ pole figures of grains shown in (b) depicted with green and red circles for prior-austenite grains 1 and 2, respectively. Also superimposed are {110}α pole figures from experimentally determined orientations in corresponding areas in (a). Please note that the colours correspond to the orientation shown in (a) and (b). One may also notice that the green and red circles, corresponding to the calculated austenite orientations, coincide with some experimental orientations of the martensitic phase and obey the NW orientation relationship {111}γ//{100}α. From the experimental pole figure, one can also observe that variant selection is present as fewer poles are present in the measured pole figure in comparison to theoretical ones.

Crack resistance of a specific crystallographic orientation may be evaluated by examining crack arrest points along the crack path. Therefore, orientation distribution function (ODF) analysis was conducted in two selected regions ahead of the crack tip and compared to one region where the crack propagated. Fig. 5d shows calculated ODFs from three regions depicted with white boxes in Fig. 5a. Texture, grain boundaries, intersection of martensite laths, segregation in addition to hydrogen-enhanced dislocation processes can affect the fracture path. As shown in the previous section, the crack initially propagated intergranulary along prior-austenite grain boundaries. The crack was arrested in region (i) when facing a $(111)[0\bar{1}1]$ texture component and was then deflected and continued to propagate transgranulary through {001} crystallographic planes which are known as cleavage planes in BCC metals [48]. The calculated ODF from region (ii) revealed that a $(001)[0\bar{1}0]$ texture component developed here. The crack finally ceased in region (iii), where a $(111)[0\bar{1}1]$ component was found. Our results indicate that the crystallographic planes {111}α have higher probability to arrest the crack, whereas crack can easily propagate through {001}α planes, which is in good agreement with results of Venegas et al. [28,29].

Refs. [28,29] also suggested that an increased proportion of coincidence site lattice related boundaries should improve the material's resistance to hydrogen-induced cracking. Therefore, coincidence site lattice boundaries distributions were analysed on EBSD maps along hydrogen-induced cracks and at crack arrest points. However, the present study found no evidence of correlation between these types of boundaries and crack propagation.

Fig. 6, upper part, shows engineering stress–strain curve for the material aged at 480 °C for 3 h obtained during loading with a strain rate of 10^{-3} s^{-1} using a Gleeble Thermomechanical Simulator integrated within the XTMS beamline at the LNLS synchrotron source. Previous works [49,50] showed that lower displacement rates during hydrogen charging tests are not necessary to induce intergranular embrittlement. X-ray synchrotron analysis of lattice strain in loaded tensile samples (specimen tested in air) revealed that the {200}α crystallographic planes accumulate approximately four times larger strain than the {222}α planes (Fig. 6, bottom part). One can also observe that with increasing of engineering strain, the lattice strain increases. The crystallographic planes that were less prone to lattice strain accumulation correlate well with crack arrest planes identified by the EBSD technique. Experimental data obtained in this study can be used to improve precision of numerical models [51,52].

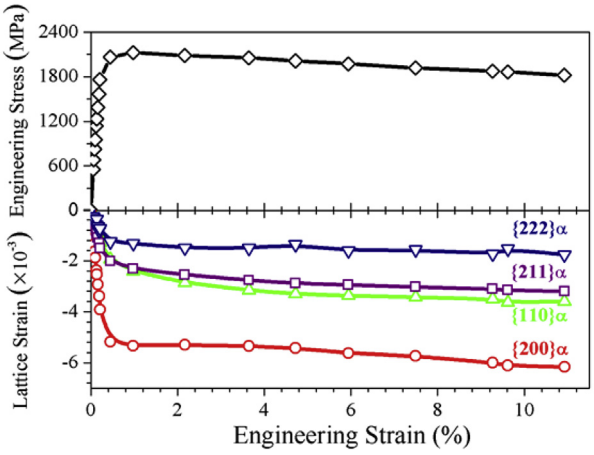

Fig. 6 – Engineering stress–strain curve of maraging steel aged at 480 °C for 3 h obtained during loading with strain rate 10^{-3} s^{-1} on Gleeble Thermomechanical Simulator integrated within XTMS synchrotron beamline, upper part of the figure. Lattice strain of individual crystallographic planes as function of engineering strain shown in the bottom part of the figure. The markers represent measurement points during synchrotron experiments. For a better clarity, colours used here correspond to the IPF colour scheme shown in Fig. 5a. (For interpretation of the references to colour in this figure legend, the reader is referred to the web version of this article.)

Conclusion

We studied HE in maraging steel that occurred during slow strain rate tensile test under hydrogen charging. HE led to significant loss in tensile ductility, producing both intergranular and transgranular cracks. Initially, cleavage was the dominant crystallographic mode of brittle fracture. The intergranular cracks were observed to propagate initially along prior-austenite grain boundaries and the fracture mode was then altered to transgranular cleavage along the {001}α//ND texture component. Cracks were finally arrested in the {111}α//ND grains.

X-ray synchrotron analysis of the lattice strain in loaded tensile samples revealed that the {200}α crystallographic planes accumulate approximately four times larger strains than the {222}α planes. The planes that were less prone to lattice strain accumulation correlate well with the crack arrest crystallographic planes identified by EBSD technique. Our findings suggest that a texture with an increased proportion of {111}α planes and a low fraction of {001}α planes could reduce crack propagation in such conditions.

Acknowledgements

The authors gratefully thank Mr. R.L. Tonoli and Dr. J. Rodríguez Fernandez for their help with diffraction data refinement and reconstruction of prior-austenite grains from EBSD maps,

respectively. Experimental support of Dr. A.L. Gobbi from Microfabrication Laboratory at Brazilian Nanotechnology National Laboratory-LNNano (Project LMF 20869) is acknowledged. This work was supported by CAPES (Project 50/2011) and CNPEM (Project 20150152). The authors acknowledge the LNNano and the Brazilian Synchrotron Light Laboratory-LNLS for the use of the XTMS installation at the XRD-1 beamline in addition to Analytical Centre – UFC/CT-INFRA/MCTI-SISNANO/Pró-Equipamentos CAPES for the use of FEG-SEM-EBSD facilities.

REFERENCES

[1] Williams DP, Nelson HG. Gaseous hydrogen embrittlement of aerospace materials. Astronaut Res 1971:323–30. Springer; 1973.
[2] Rao MN, Mohan MK, Reddy PUM. Environmentally assisted cracking of 18% Ni maraging steel. Corros Sci 2009;51:1645–50.
[3] Wang G, Yan Y, Li J, Huang J, Qiao L, Volinsky AA. Microstructure effect on hydrogen-induced cracking in TM210 maraging steel. Mater Sci Eng A 2013;586:142–8.
[4] Nagao A, Smith CD, Dadfarnia M, Sofronis P, Robertson IM. The role of hydrogen in hydrogen embrittlement fracture of lath martensitic steel. Acta Mater 2012;60(13–14):5182–9.
[5] Tiwari GP, Bose A, Chakravartty JK, Wadekar SL, Totlani MK, Arya RN, et al. A study of internal hydrogen embrittlement of steels. Mater Sci Eng A 2000;286:269–81.
[6] Yan Y, Yan Y, He Y, Li J, Su Y, Qiao L. Hydrogen-induced cracking and service safety evaluation for precipitation strengthened austenitic stainless steel as hydrogen storage tank. Int J Hydrogen Energy 2014;39:17921–8.
[7] Sun Z, Benoit G, Moriconi C, Hamon F, Halm D, Hénaff G. Fatigue crack propagation under gaseous hydrogen in a precipitation-hardened martensitic stainless steel. Int J Hydrogen Energy 2011;36:8641–4.
[8] Beachem CD. A new model for hydrogen-assisted cracking (Hydrogen "embrittlement"). Metal Trans 1972;3:441–55.
[9] Marchetti L, Herms E, Laghoutaris P, Chêne J. Hydrogen embrittlement susceptibility of tempered 9% Cr–1% Mo steel. Int J Hydrogen Energy 2011;36:15880–7.
[10] Michler T, Naumann J. Hydrogen embrittlement of Cr-Mn-N-austenitic stainless steels. Int J Hydrogen Energy 2010;35:1485–92.
[11] Takasawa K, Ikeda R, Ishikawa N, Ishigaki R. Effects of grain size and dislocation density on the susceptibility to high-pressure hydrogen environment embrittlement of high-strength low-alloy steels. Int J Hydrogen Energy 2012;37:2669–75.
[12] Robertson IM, Sofronis P, Nagao A, Martin ML, Wang S, Gross DW, et al. Hydrogen embrittlement understood. Metal Mater Trans A 2015;46:2323–41.
[13] Niwa M, Shikama T, Yonezu A. Mechanism of hydrogen embrittlement cracking produced by residual stress from indentation impression. Mater Sci Eng A 2015;624:52–61.
[14] Yonezu A, Hara T, Kondo T, Hirakata H, Minoshima K. Evaluation of threshold stress intensity factor of hydrogen embrittlement cracking by indentation testing. Mater Sci Eng A 2012;531:147–54.
[15] Koyama M, Akiyama E, Tsuzaki K, Raabe D. Hydrogen-assisted failure in a twinning-induced plasticity steel studied under in situ hydrogen charging by electron channeling contrast imaging. Acta Mater 2013;61:4607–18.
[16] Nagumo M. Function of hydrogen in embrittlement of high-strength steels. ISIJ Int 2001;41:590–8.
[17] Oriani RA. A mechanistic theory of hydrogen embrittlement of steels. Ber Bunsenges Phys Chem 1972;76:848–57.
[18] Birnbaum HK, Sofronis P. Hydrogen-enhanced localized plasticity-a mechanism for hydrogen-related fracture. Mater Sci Eng A 1994;176:191–202.
[19] Michler T, Naumann J. Microstructural aspects upon hydrogen environment embrittlement of various bcc steels. Int J Hydrogen Energy 2010;35:821–32.
[20] Zhu X, Li W, Zhao H, Wang L, Jin X. Hydrogen trapping sites and hydrogen-induced cracking in high strength quenching & partitioning (Q&P) treated steel. Int J Hydrogen Energy 2014;39:13031–40.
[21] Nagao A, Smith CD, Dadfarnia M, Sofronis P, Robertson IM. The role of hydrogen in hydrogen embrittlement fracture of lath martensitic steel. Acta Mater 2012;60:5182–9.
[22] Momotani Y, Shibata A, Terada D, Tsuji N. Effect of strain rate on hydrogen embrittlement in low carbon martensitic steel. Int Symp New Dev Adv High Strength Sheet Steels 2013:303–9.
[23] Kim YH, Morris JW. The nature of quasicleavage fracture in tempered 5.5 Ni steel after hydrogen charging. Metall Trans A 1983;14:1883–8.
[24] Latanision RM, Opperhauser H. The intergranular embrittlement of nickel by hydrogen: the effect of grain boundary segregation. Metall Trans 1974;5:483–92.
[25] Davies PA, Novovic M, Randle V, Bowen P. Application of electron backscatter diffraction (EBSD) to fracture studies of ferritic steels. J Microsc 2002;205:278–84.
[26] Qiao Y, Argon AS. Cleavage cracking resistance of high angle grain boundaries in Fe–3% Si alloy. Mech Mater 2003;35:313–31.
[27] Venegas V, Caleyo F, González JL, Baudin T, Hallen JM, Penelle R. EBSD study of hydrogen-induced cracking in API-5 L-X46 pipeline steel. Scr Mater 2005;52:147–52.
[28] Venegas V, Caleyo F, Hallen JM, Baudin T, Penelle R. Role of crystallographic texture in hydrogen-induced cracking of low carbon steels for sour service piping. Metall Mater Trans A 2007;38:1022–31.
[29] Venegas V, Caleyo F, Baudin T, Espina-Hernandez JH, Hallen JM. On the role of crystallographic texture in mitigating hydrogen-induced cracking in pipeline steels. Corros Sci 2011;53:4204–12.
[30] Mohtadi-Bonab MA, Szpunar JA, Basu R, Eskandari M. The mechanism of failure by hydrogen induced cracking in an acidic environment for API 5L X70 pipeline steel. Int J Hydrogen Energy 2015;40:1096–107.
[31] Bechtle S, Kumar M, Somerday BP, Launey ME, Ritchie RO. Grain-boundary engineering markedly reduces susceptibility to intergranular hydrogen embrittlement in metallic materials. Acta Mater 2009;57:4148–57.
[32] Venegas V, Caleyo F, Herrera O, Hernández-Sánchez J, Hallen JM. Crystallographic texture helps reduce hydrogen induced cracking in pipeline steels. Int J Electrochem Sci 2014;9:418–25.
[33] Rugg D, Dixon M, Dunne FPE. Effective structural unit size in titanium alloys. J Strain Anal Eng Des 2007;42:269–79.
[34] Lee SY, Choo H, Liaw PK, Oliver EC, Paradowska AM. In situ neutron diffraction study of internal strain evolution around a crack tip under variable-amplitude fatigue-loading conditions. Scr Mater 2009;60:866–9.
[35] Blondé R, Jimenez-Melero E, Zhao L, Wright JP, Bru E, Van der Zwaag S, et al. High-energy X-ray diffraction study on the temperature-dependent mechanical stability of retained austenite in low-alloyed TRIP steels. Acta Mater 2012;60:565–77.
[36] Farooq M, ul Haq A, Hashmi FH, Khan AQ. Microscopic determination of austenite in 18% Ni maraging steel. Metallography 1987;20:377–83.

[37] ASTM Standard G129-00. Standard practice for slow strain rate testing to evaluate the susceptibility of metallic materials to environmentally assisted cracking. American Society for Testing and Materials; 2000.
[38] ASTM Standard F1624-09. Standard test method for measurement of hydrogen embrittlement threshold in steel by the incremental step loading technique. American Society for Testing and Materials; 2009.
[39] Santos LPM, Béreš M, Bastos IN, Tavares SSM, Abreu HFG, da Silva MJG. Hydrogen embrittlement of ultra high strength 300 grade maraging steel. Corros Sci 2015;101:12–8.
[40] Cayron C. ARPGE: a computer program to automatically reconstruct the parent grains from electron backscatter diffraction data. J Appl Crystallogr 2007;40:1183–8.
[41] Bachmann F, Hielscher R, Schaeben H. Texture analysis with MTEX–free and open source software toolbox. Solid State Phenom 2010;160:63–8.
[42] Viswanathan UK, Dey GK, Sethumadhavan V. Effects of austenite reversion during overageing on the mechanical properties of 18 Ni (350) maraging steel. Mater Sci Eng A 2005;398:367–72.
[43] Gerberich WW, Chen XF, Kaczorowski M. Crack growth from internal hydrogen-Temperature and microstructural effects in 4340 steel. Metall Trans A 1988;19:1319–34.
[44] Ohtani H, McMahon CJ. Modes of fracture in temper embrittled steels. Acta Metall 1975;23:377–86.
[45] Wei RP, Simmons GW. A technique for determining the elemental composition of fracture surfaces produced by crack growth in hydrogen and in water vapor. Scr Metall 1976;10:153–7.
[46] Fuchigami H, Minami H, Nagumo M. Effect of grain size on the susceptibility of martensitic steel to hydrogen-related failure. Philos Mag Lett 2006;86:21–9.
[47] Figueroa D, Robinson MJ. Hydrogen transport and embrittlement in 300M and AerMet100 ultra high strength steels. Corros Sci 2010;52:1593–602.
[48] Pineau A, Benzerga AA, Pardoen T. Failure of metals I: brittle and ductile fracture. Acta Mater 2016;107:424–83.
[49] Lassila DH, Birnbaum HK. Intergranular fracture of nickel: the effect of hydrogen-sulfur co-segregation. Acta Metall 1987;35:1815–22.
[50] Seifi M, Holroyd NJH, Lewandowski JJ. Deformation rate and sensitization effects on environmentally assisted cracking of Al-Mg naval alloys. Corrosion 2016;72(2):264–83.
[51] Novotný L. Calculation of T – stress on 3D specimens with crack. Procedia Eng 2012;48:489–94.
[52] Halama M, Jerolitsch D, Žilková J, Dzedzina R, Linhardt P. Improvement of ENANOCS technique using artificial neural networks approach for the detection of corrosion. Eurocorr, MAKC Press; 2010. p. 1–8.